

New polymorphic phase and rich phase diagram in the PdSe_{2-x}Te_x system

Wenhao Liu¹, Mehrdad Rostami Osanloo¹, Xiqu Wang³, Sheng Li¹, Nikhil Dhale¹, Hanlin Wu¹,
Maarten L. Van de Put², William G. Vandenberghe², Bing Lv^{1,2*}

1. Department of Physics, The University of Texas at Dallas, Richardson, Texas 75080, USA
2. Department of Materials Science and Engineering, The University of Texas at Dallas, Richardson, Texas 75080, USA
3. Department of Chemistry, University of Houston, Houston Texas 77004, USA

* to whom the correspondence should be addressed: blv@utdallas.edu

Abstract

We report a combined experimental and theoretical study of the PdSe_{2-x}Te_x system. With increasing Te fraction, structural evolutions, first from an orthorhombic phase (space group *Pbca*) to a monoclinic phase (space group *C2/c*) and then to a trigonal phase (space group *P-3m1*), are observed accompanied with clearly distinct electrical transport behavior. The monoclinic phase (*C2/c*) is a completely new polymorphic phase and is discovered within a narrow range of Te composition ($0.30 \leq x \leq 0.80$). This phase has a different packing sequence from all known transition metal dichalcogenides to date. Electronic calculations and detailed transport analysis of the new polymorphic PdSe_{1.3}Te_{0.7} phase are presented. In the trigonal phase region, superconductivity with enhanced critical temperature is also observed within a narrow range of Te content ($1.0 \leq x \leq 1.2$). The rich phase diagram, new polymorphic structure as well as abnormally enhanced superconductivity could further stimulate more interest to explore new types of polymorphs and investigate their transport and electronic properties in the transition metal dichalcogenides family that are of significant interest.

Introduction

The study of a variety of polymorphic structures of transition metal dichalcogenides (TMDs), and the discoveries of their unique properties through atomic-scale structure control, have emerged as a research frontier of science for new exciting physics as well as miniaturizing of electronic devices, energy conversion and storage¹⁻⁹. TMD polymorphs are chemically rather simple and structured with fundamental MX₂ layers where M is a transition metal (such as V, Nb, Ta, Ti, Zr, Hf, Mo, W, Pd, and Pt) and X is a chalcogen atom (such as S, Se, or Te)¹⁰. With strong in-plane bonding and weak out-of-plane van der Waals interactions, these materials can be easily exfoliated down to atomic thickness, and thus enable bottom-up atomic-scale structure control and unique stacking/twisting to reveal new physics or novel functionalities¹¹⁻¹³.

The research of various structures of TMDs have a long and fruitful history. Various polymorphic structures appear starting from either the trigonal prismatic or the octahedral coordination of the metal atoms. Depending on the different stacking order of atomic planes and possible distortions, the most commonly encountered arrangements are 1T (T: trigonal), 2H (H: hexagonal), 3R (R: rhombohedral), 1T' (distorted 1T into monoclinic phase), and T_d (distorted 1T into orthorhombic phase)¹⁴⁻¹⁸. The digits (1-3) indicate the number of layers in the stacking sequence in the primitive unit cell.

The different polymorphs in TMDs often display drastically different physical phenomena. For example, three different polymorphs showing distinct properties are found for the MoTe₂ phases: 2H-MoTe₂ shows semiconducting behaviors with a bandgap of about 1.1 eV, 1T'-MoTe₂ has a metallic behavior^{19,20}, and T_d-MoTe₂ is topologically nontrivial and a candidate Weyl semimetal^{21,22}. Another example is found in the

TaSe_{2-x}Te_x system, where various polymorphic structures have been observed. With increasing Te concentration, the material appears as an incommensurate charge-density-wave (ICDW) 2H-TaSe₂ phase, as a 3R phase with a maximal superconducting transition temperature (T_c) of 2.4K, as a different 1T phase (also superconducting with lower T_c at 0.5-0.7 K), and finally as a normal metallic monoclinic TaTe₂ phase²³.

Interestingly, PdS₂ and PdSe₂, less studied TMDs, have a puckered pentagonal configuration with orthorhombic space group *Pbca* shown in Fig. 1(a). The *Pbca* space group is rarely found in TMDs and hosts pentagons. Pentagons are often considered as topological defects or geometrical frustrations²⁴. Pentagonal graphene and SnS₂ have been theoretically predicted to possess quite unique physical properties, such as unusual negative Poisson's ratio or a room-temperature quantum spin Hall insulator state^{25,26}. Different from the other TMDs where the metal coordination is either trigonal prismatic or octahedral (sometimes distorted), the Pd metal configuration in PdS₂ and PdSe₂ are in fact rectangular nets. PdSe₂ is highly stable in air down to the monolayer limit²⁷. The bandgap varies greatly from 0.5 eV in bulk to 1.37 eV in monolayers, and the thin PdSe₂ field-effect transistors exhibit intrinsic ambipolar characteristic and high electron mobility^{28,29}. Under high pressure, bulk PdSe₂ transforms from a pentagonal layered structure to a pyrite type structure and superconductivity up to 13.1 K emerges, which is the highest critical temperature (T_c) among all the TMD materials to date³⁰. On the other hand, PdTe₂ adopts the layered 1T structure with space group *P-3m1* (Fig.1(b)). PdTe₂ has an octahedral (i.e. trigonal antiprismatic) coordination, is metallic, and is characterized by an ABC Se-Pd-Se stacking order within the layer. Dirac semimetal and superconductivity with T_c of 1.65 K have been experimentally verified to coexist in PdTe₂³¹⁻³³.

The distinct difference in structure and electronic properties of PdSe₂ and PdTe₂ motivate us to explore the possible structural evolution/transformation, and their associated electrical transport behavior changes in the PdSe_{2-x}Te_x system. We have demonstrated previously that the superconductivity of PdTe₂ can be enhanced up to 2.73 K when half of the Te in PdTe₂ is replaced by Se atoms³⁴. Here, we study the full range of the PdSe_{2-x}Te_x ($0 \leq x \leq 2$) system and discover a new *C2/c* polymorphic structure with similar building unit as 1T PdTe₂. We complement our experimental results with theoretical first principles calculations. The PdSe₂-PdTe₂ phase diagram and associated electrical transport results, including superconductivity, are presented.

Results and discussions

1. Structure evolution

Fig. 2(a) shows the X-ray diffraction patterns for PdSe_{2-x}Te_x samples. At first glance, one can clearly observe three different types of structures with one of the corresponding characteristic peaks highlighted in the Fig. 2(a). In the Se rich region $0 \leq x \leq 0.3$, the XRD peaks shifts slightly towards lower angle, as expected with increasing Te content, and the PdSe_{2-x}Te_x maintains the puckered pentagonal PdSe₂ structure with orthorhombic lattice. A second phase starts to emerge at $x = 0.3$, although the major phase remains the PdSe₂ structure, this new phase becomes more dominant when $x \geq 0.5$ and coexists with the PdSe₂-type phases until $x = 0.6$. In the composition range of $0.7 \leq x \leq 0.8$, an XRD pure quality of the new phase was obtained. With further increasing of the Te content for $0.9 \leq x \leq 2.0$, the structure transformed to the *P-3m1*(1T) structure. Fig. 2(b) and Fig. 2(c) are the Rietveld refinement results for the PdSe_{1.9}Te_{0.1} and PdSe_{0.6}Te_{1.4} samples. The refined lattice parameters for PdSe_{1.9}Te_{0.1} are $a = 5.7687(2)$ Å $b = 5.8973(6)$ Å $c = 7.7160(8)$ Å, which are slightly bigger than those of PdSe₂ ($a = 5.7410$ Å $b = 5.8660$ Å $c = 7.6910$ Å) as

expected. The refined lattice parameters for the $\text{PdSe}_{0.6}\text{Te}_{1.4}$ sample are $a = b = 3.9460(9)$ Å and $c = 5.0371(5)$ Å, slightly less than that of CdI_2 -type PdTe_2 as Se atoms are smaller than Te atoms.

A small crystal from the $\text{PdSe}_{1.2}\text{Te}_{0.8}$ sample is selected for the X-ray single crystal diffraction. The determined crystallographic parameters, refinement details, atomic coordinates, occupancies and equivalent anisotropic displacement parameters are included in Table 1. The refined ratio of $\text{Se}:\text{Te} = 1.23(2):0.77(2)$, is rather close to the nominal composition and consistent with the chemical analysis results from SEM analysis. The crystal structure of the refined $\text{PdSe}_{1.23(2)}\text{Te}_{0.77(2)}$ is shown in Fig. 3(a). The refined $\text{PdSe}_{1.23(2)}\text{Te}_{0.77(2)}$ crystallizes in a new polymorphic structure in a monoclinic cell with space group $C2/c$ (#15), the chalcogen-chalcogen interlayer interactions now appear as covalent bonds, and a three-dimensional framework is visualized in Fig. 3(a). The chalcogen-Pd-chalcogen stacking is maintained similar stacking order with a fundamental building motif $\text{Pd}(\text{Se},\text{Te})_6$ octahedra, just like in the 1T PdTe_2 phase. However, the $\text{Pd}(\text{Se},\text{Te})_6$ octahedra are much more distorted, and severely elongated along one direction within the plane, compared to the PdTe_6 octahedra in PdTe_2 , as is shown in the Fig. 4(b). As a result, the chalcogen-chalcogen distance between the adjacent stacking layers decreases down to $2.6338(5)$ Å in the $\text{PdSe}_{1.23(2)}\text{Te}_{0.77(2)}$ from the value of 3.463 Å in the 1T- PdTe_2 system, suggesting an effective covalent bonding interaction between the two adjacent layers. Another distinct difference of this new polymorphic phase from PdSe_2 and PdTe_2 is on the Pd metal configurations. As shown in the Fig. 3(c), the Pd metals in the new polymorphic phase $\text{PdSe}_{1.23(2)}\text{Te}_{0.77(2)}$ have a rhombus packing with an obtuse angle measuring $\sim 117^\circ$, which is completely different from the rectangular Pd packing (*i.e.*, 90°) in the PdSe_2 and trigonal antiprismatic Pd packing (*i.e.*, 120°) in the PdTe_2 structure. The Pd-Pd distance is ~ 3.99 Å, which is smaller than 4.10 Å in the PdSe_2 phase and 4.04 Å in the PdTe_2 phase.

Fig. 4 shows the formation energy for $\text{PdSe}_{2-x}\text{Te}_x$, in the $Pbca$ phase, the $C2/c$ phase and the $P-3m1$ phase, calculated using DFT. The theoretical calculations show that the $Pbca$ phase is the most stable phase for $x=0$ (PdSe_2), for $x=0.3$ up to $x=0.8$, the $C2/c$ phase appears the most stable, and for $x > 0.8$, the $P-3m1$ phase has the lowest energy. These results are in excellent agreement with the experimentally grown material, characterized by the X-ray diffraction results shown in Fig. 2. Overall, the agreement is remarkable although a slight discrepancy between theory and experiment is observed in the $x = 0.3$ to $x = 0.6$ region where experimentally both the $Pbca$ and the $C2/c$ co-exist while our theoretical calculations clearly favor the $C2/c$ phases. We note that the phonon contribution is a significant component to the Gibbs free energy and our theoretical results reveal that the entropy associated with the phonons is an important component in determining which phase is most stable.

As far as we know, the $C2/c$ structure has not been previously reported for TMDs. This unique polymorphic structure, through this novel Pd packing and PdSe_6 stacking, could offer another promising platform to investigate interesting structural and electrical behaviors near the critical point of two- and three-dimensionality.

2. Electronic properties

Fig. 5 shows the changes of electrical transport properties in the $\text{PdSe}_{2-x}\text{Te}_x$ system upon Te doping. As one can see from Fig. 5(a), a clear crossover in electrical transport accompanied by the semiconductor-to-metal transition is observed with increasing Te content. Fig.5(b) shows the plot of $\ln(\rho/\rho_{300\text{K}})$ vs $(1/T)$ for a $\text{PdSe}_{1.9}\text{Te}_{0.1}$ sample, where thermally activated conduction behavior is observed. Two clear linear relations of $\ln(\rho/\rho_{300\text{K}})$ vs. $(1/T)$ are found in the range of 140-300 K and 30-69 K, indicating an energy gap of 92 meV and 13 meV, respectively. Fig. 5(c) shows the temperature dependent electrical resistivity $\rho(T)$ for the new polymorphic phase of $\text{PdSe}_{1.3}\text{Te}_{0.7}$. The resistivity value is weakly dependent on the temperature and

shows an overall semiconducting behavior from room temperature down to 50 K. An anomalous kink arises at the temperature ~ 50 K and a clear slope change of resistivity is observed afterwards. The resistivity increases more gently and has a tendency of saturation below 50 K, which may be related with the weak localizations of electrons caused by the disorders in this system.

The semiconducting behavior of the new phase is also verified with theoretical DFT calculations. Fig. 6 shows the calculated band structure and density-of-states (DOS) of $\text{PdSe}_{1.25}\text{Te}_{0.75}$. The DFT results show a small (15 meV) indirect bandgap for the $C2/c$ phase in agreement with the experimental transport measurements. The conduction band minimum appears at the S point while the valence band maximum appears along the Γ -Y line. We also found that without the on-site electron-electron interaction ($U = 4$ eV) no band gap was observed.

The inset of Fig. 5(c) highlights the plot of $\ln \rho$ vs $(1/T)$ below 50K. The curves become almost T -independent at low temperature between 2 and 30K, indicating the existence of a hopping process in the materials. Several general hopping models could contribute to the electrical transport in $\text{PdSe}_{2-x}\text{Te}_x$. One is the nearest-neighbor hopping model (NNH) where ρ is proportional to $\exp(E_A/k_B T)$. Here E_A is the activation energy and k_B is the Boltzmann constant³⁵. Another model describes variable range hopping (VRH) where $\rho \propto [\exp(T_0/T)]^{1/(1+d)}$ and often occurs between states with larger spatial distance but closer energy³⁶. Here T_0 is a characteristic temperature and d is the dimensionality of the solid-state materials. VRH has been found in many disordered systems³⁷⁻³⁹.

In our system, one can clearly observe that the slope decreases continuously with decreasing temperature, which suggests the existence of multiple conducting channels. Therefore, we utilized one NNH model together with one VRH model to fit our low temperature resistivity data below 50 K using the following equation:

$$R(T)^{-1} = R_0^{-1} + R_1^{-1} \exp[-E_1/2k_B T] + R_2^{-1} \exp\left[-(T_2/T)^{\frac{1}{3}}\right] \quad [1]$$

Where E_1 is the activation energy, T_2 is the characteristic temperature, R_0 , R_1 and R_2 are the related resistance coefficients. Here the temperature independent R_0^{-1} represent the scattering of electrons by disorders in low temperature. The extracted activation energy E_1 is about 2 meV. The low activation energy E_1 reveals inhomogeneous localization-distributions in this system and the nearly free carriers are weakly localized by the disorder. When the temperature decreases below 30 K, the VRH dominates and the characteristic temperature is extracted to be $\sim 4.8 \times 10^4$ K. Here the characteristic temperature has a positive relation with the optimal hopping distance of the localized electrons and the yielding value is consistent with many other TMD materials³⁹. We have also tried to fit out data with 1D, 2D and 3D VRH models and all of them fail to converge. When combining one NNH with a VRH model of 1D and 3D no convergence on the fit is observed either. The fact that only the 2D VRH combined with the NNH mode fits the data well, suggests that the structure of this new polymorphic phase is closer to quasi-2D rather than 3D.

Fig. 5(d) shows the temperature dependence of the Hall resistivity ρ_{xy} for $\text{PdSe}_{1.3}\text{Te}_{0.7}$, exhibiting the new $C2/c$ phase, at 10, 30, 60, 100, 150 and 200 K. Here ρ_{xy} shows linearly dependent behaviors with the magnetic field. The slopes are all negative, indicating that the charge carriers are dominantly electrons near the Fermi surface. The Hall coefficient $R_H = \rho_{xy}/\mu_0 H$ estimated by the linearly fitting of ρ_{xy} , is shown in the inset of Fig. 4(d). R_H scales almost monotonically with temperature and there are no significant changes of R_H around 50 K. The charge-carrier density is estimated to be $5.12 \times 10^{19} \text{ cm}^{-3}$ at 10 K, which is about 2 orders smaller than the $5.5 \times 10^{21} \text{ cm}^{-3}$ extracted for PdTe_2 in Ref.³³.

Finally, Fig. 5(e) and 5(f) show the temperature dependence of the in-plane resistivity ratio ρ/ρ_{300K} of $\text{PdSe}_{2-x}\text{Te}_x$ samples with x in the range $0.9 \leq x \leq 1.5$. All of these samples show metallic behavior with residual resistivity ratios (RRR) around 2, which are smaller than 75 of the PdTe_2 single crystal⁴⁰, reflecting the substantial disorder induced by Te substitution. Remarkably, in the composition range $1.0 \leq x \leq 1.2$, superconductivity suddenly occurs with an onset T_c close to 2.7 K. For compositions beyond $x > 1.2$, no superconductivity is detected above 1.8 K (the limit of our instrument), but the samples could possibly still be superconducting below 1.8 K, as 1T- PdTe_2 is superconducting at 1.65 K.

3. Phase diagram

Fig. 7 summarizes the rich phase diagram for the $\text{PdSe}_{2-x}\text{Te}_x$ system where both crystal symmetry and lattice parameters are listed. With increasing Te content x , the structure of $\text{PdSe}_{2-x}\text{Te}_x$ retains an orthorhombic phase up to $x = 0.3$. A new monoclinic polymorphic phase starts to emerge when $x \geq 0.3$ and remains stable up to $x = 0.8$. With further doping beyond $x = 0.9$, the monoclinic phase becomes unstable and the samples transform to a $P-3m1$ (1T) phase. Within a narrow region of $P-3m1$ (1T) phase when $1.0 \leq x \leq 1.2$, the samples show superconductivity with onset T_c close to 2.7 K, as reported by us previously³⁴.

In conclusion, we have carried out a systematic study of isoelectronic substitution of Te for Se in $\text{PdSe}_{2-x}\text{Te}_x$ solid solutions. A structural evolution with increasing Te fraction from the $Pbca$ PdSe_2 phase to the $P-3m1$ PdTe_2 phase was observed accompanied with clearly distinct electrical transport behavior. A completely new polymorphic $C2/c$ structure was discovered within a narrow range of Te composition ($x = 0.3$ to $x = 0.8$), and the $C2/c$ structure has a distinct packing structure which is different from all known TMDs to date. Theoretical first principles calculations agree with the experimental findings and revealed that the phonon-contribution to the free energy is an important factor in making the $Pbca$ and $C2/c$ favorable phases. The $C2/c$ phase showed electron-dominated charge carriers and displayed an unusual electrical conductivity behavior which could be well explained through the combined nearest-range-hopping and variable-range-hopping model. In the $P-3m1$ (1T) phase region, an enhanced superconductivity emerges in a narrow range with onset T_c about 2.7 K. The rich phase diagram and new polymorphic structure discovered in this system could provide a new material platform to further investigate transport and electronic properties of different types of polymorphs in the TMD structure that of significant interest.

Methods

A. Experimental method

The $\text{PdSe}_{2-x}\text{Te}_x$ crystals were synthesized using self-flux methods. Pd ingots (99.95%, Alfa Aesar), Se shots (99.999%, Alfa Aesar) and Te pieces (99.999%, Alfa Aesar) were mixed in the right stoichiometric doping ratio in an Ar glovebox with a total moisture and oxygen level less than 0.1 ppm. The source elements were loaded inside a silica tube, which was then flame sealed under vacuum and placed in a box furnace. The temperature was slowly increased to 800 °C, held for three days and followed by furnace cooling down to room temperature.

Chemical composition of the yield crystals was verified by energy-dispersive X-ray spectroscopy (EDX) on a DM07 Zeiss Supra 40 Scanning Electron Microscope. Powder X-ray diffraction (XRD) measurements were carried out at room temperature on crushed crystals using a Rigaku SmartLab X-ray diffractometer equipped with Cu-K α radiation. Rietveld refinement was carried out using GSAS-II⁴¹. Resistivity was measured using the four-probe method in a Quantum Design Physical Property Measurement System

(PPMS) down to 1.8 K. Four gold wires (30 μm in diameter) were pasted on the sample surface by silver epoxy as four probes.

The crystal structure of the new $\text{PdSe}_{1.2}\text{Te}_{0.8}$ phase was determined with single crystal X-ray data measured on a Bruker SMART diffractometer equipped with an Apex II area detector and an Oxford Cryosystems 700 Series temperature controller with a $\text{Mo } K\alpha$ source ($\lambda = 0.71073\text{\AA}$). The collected dataset was integrated using the Bruker Apex-II program, with the intensities corrected for the Lorentz factor, polarization, air absorption, and absorption due to variation in the path length through the detector faceplate. The data was scaled, and absorption correction was applied using SADABS. The structure was solved by using the intrinsic phasing method in SHELXT and refined using SHELXL with all atoms refined anisotropically.

B. Theoretical model

The theoretical calculations are based on Density Functional Theory (DFT) as implemented in Vienna ab initio simulation package (VASP)⁴². To correctly account for the van der Waals forces, we employed the non-local optPBE-vdW functionals proposed by Dion *et al.*⁴³ with parameters by Oyedele *et al.* and Klimeš *et al.*^{24,44}. Electron correlation effects in the d-orbitals of Pd were accounted for in the PBE+ U approximation with $U = 4$ eV. To study various compositions of $\text{PdSe}_{2-x}\text{Te}_x$, we used $2 \times 2 \times 1$ supercells, providing 8 compositions of $x = \left\{0, \frac{1}{4}, \frac{1}{2}, \frac{3}{4}, 1, \frac{5}{4}, \frac{3}{2}, \frac{7}{4}, 2\right\}$. The Brillouin zone was sampled with a Γ -centered Monkhorst-Pack grid of $10 \times 10 \times 6$, $6 \times 12 \times 10$, and $15 \times 15 \times 3$ k-points, for the $Pbca$, $C2/c$, and $P-3m1$ structures, respectively. The electronic wave functions were expanded in a plane-wave basis with a kinetic-energy cutoff of 325 eV. The atomic positions of each composition were optimized until the force on each atom was lower than 10^{-3} eV/ \AA and the total energy was accurate to 10^{-8} eV.

After optimization, the intra-layer bond-length and inter-layer distance was measured. The Gibbs free energy of each structure and composition was calculated using:

$$G = E_0 - TS_{\text{vibr}},$$

where E_0 is the ground state energy calculated from DFT and $E_{\text{vibr}} = TS_{\text{vibr}}$ is the vibrational Gibbs free energy associated with the phonon frequencies ω_i through

$$E_{\text{vibr}} = \sum_i \left\{ \frac{\hbar\omega_i}{2} + k_B T \ln \left[1 - \exp\left(-\frac{\hbar\omega_i}{k_B T}\right) \right] \right\}.$$

The formation energy was calculated as the difference between the Gibbs free energy of the compound and of the elemental metals, evaluated at $T = 300\text{K}$,

$$G_{\text{form}} = G_{\text{PdSe}_{2-x}\text{Te}_x} - G_{\text{Pd}} - (2-x) G_{\text{Se}} - x G_{\text{Te}}.$$

Finally, the exfoliation energy of $\text{PdSe}_{2-x}\text{Te}_x$ was estimated as the difference between the ground state energies (E_0) of the bulk and monolayers forms per unit of surface area.

1. Fiori, G. *et al.* Electronics based on two-dimensional materials. *Nat. Nanotechnol.* **9**, 768–779 (2014).
2. Novoselov, K. S., Mishchenko, A., Carvalho, A. & Castro Neto, A. H. 2D materials and van der Waals heterostructures. *Science* **353**, aac9439 (2016).

3. Yun, Q. *et al.* Layered Transition Metal Dichalcogenide-Based Nanomaterials for Electrochemical Energy Storage. *Adv. Mater.* **32**, 1903826 (2020).
4. Wang, Q. H., Kalantar-Zadeh, K., Kis, A., Coleman, J. N. & Strano, M. S. Electronics and optoelectronics of two-dimensional transition metal dichalcogenides. *Nat. Nanotechnol.* **7**, 699–712 (2012).
5. Choi, W. *et al.* Recent development of two-dimensional transition metal dichalcogenides and their applications. *Mater. Today* **20**, 116–130 (2017).
6. Zhang, Y. *et al.* Superconductivity Series in Transition Metal Dichalcogenides by Ionic Gating. *Sci. Rep.* **5**, 12534 (2015).
7. Ciarrocchi, A., Avsar, A., Ovchinnikov, D. & Kis, A. Thickness-modulated metal-to-semiconductor transformation in a transition metal dichalcogenide. *Nat. Commun.* **9**, 919 (2018).
8. Li, J. *et al.* General synthesis of two-dimensional van der Waals heterostructure arrays. *Nature* **579**, 368–374 (2020).
9. Wu, S. *et al.* Observation of the quantum spin Hall effect up to 100 kelvin in a monolayer crystal. *Science* **359**, 76–79 (2018).
10. Chhowalla, M. *et al.* The chemistry of two-dimensional layered transition metal dichalcogenide nanosheets. *Nat. Chem.* **5**, 263–275 (2013).
11. Jin, C. *et al.* Observation of moiré excitons in WSe₂/WS₂ heterostructure superlattices. *Nature* **567**, 76–80 (2019).
12. Ulstrup, S. *et al.* Direct observation of minibands in a twisted graphene/WS₂ bilayer. *Sci. Adv.* **6**, eaay6104 (2020).
13. Wang, L. *et al.* Correlated electronic phases in twisted bilayer transition metal dichalcogenides. *Nat. Mater.* **19**, 861–866 (2020).
14. Li, Q. *et al.* Proximity-Induced Superconductivity with Subgap Anomaly in Type II Weyl Semi-Metal WTe₂. *Nano Lett.* **18**, 7962–7968 (2018).
15. Zhong, H. X., Gao, S., Shi, J. J. & Yang, L. Quasiparticle band gaps, excitonic effects, and anisotropic optical properties of the monolayer distorted 1T diamond-chain structures ReS₂ and ReSe₂. *Phys. Rev. B.* **92**, 115438 (2015).
16. Brown, B. E. The crystal structures of NbTe₂ and TaTe₂. *Acta Crystallogr.* **20**, 264–267 (1966).
17. Deng, Y. *et al.* Controlled Growth of 3R Phase Tantalum Diselenide and Its Enhanced Superconductivity. *J. Am. Chem. Soc.* **142**, 2948–2955 (2020).
18. Einar Bjerkelund, A. K. On the Structural Properties of Ta_{1+x}Se₂ Phase. **21**, 513 (1965).
19. Yan, B. & Felser, C. Topological Materials: Weyl Semimetals. *Annu. Rev. Condens. Matter Phys.* **8**, 337–354 (2017).
20. Empante, T. A. *et al.* Chemical Vapor Deposition Growth of Few-Layer MoTe₂ in the 2H, 1T', and 1T Phases: Tunable Properties of MoTe₂ Films. *ACS Nano* **11**, 900–905 (2017).

21. Sankar, R. *et al.* Polymorphic Layered MoTe₂ from Semiconductor, Topological Insulator, to Weyl Semimetal. *Chem. Mater.* **29**, 699–707 (2017).
22. Jiang, J. *et al.* Signature of type-II Weyl semimetal phase in MoTe₂. *Nat. Commun.* **8**, 13973 (2017).
23. Luo, H. *et al.* Polytypism, polymorphism, and superconductivity in TaSe₂ - XTe_x. *Proc. Natl. Acad. Sci. U. S. A.* **112**, E1174–E1180 (2015).
24. Oyedele, A. D. *et al.* PdSe₂: Pentagonal Two-Dimensional Layers with High Air Stability for Electronics. *J. Am. Chem. Soc.* **139**, 14090–14097 (2017).
25. Yu, Y. *et al.* Gate-tunable phase transitions in thin flakes of 1T-TaS₂. *Nat. Nanotechnol.* **10**, 270–276 (2015).
26. Ma, Y., Kou, L., Li, X., Dai, Y. & Heine, T. Room temperature quantum spin Hall states in two-dimensional crystals composed of pentagonal rings and their quantum wells. *NPG Asia Mater.* **8**, e264 (2016).
27. Yu, P. *et al.* PdSe₂: Pentagonal Two-Dimensional Layers with High Air Stability for Electronics. *J. Am. Chem. Soc.* **139**, 14090–14097 (2017).
28. Chow, W. L. *et al.* High Mobility 2D Palladium Diselenide Field-Effect Transistors with Tunable Ambipolar Characteristics. *Adv. Mater.* **29**, 1602969 (2017).
29. Zhang, G. *et al.* Optical and electrical properties of two-dimensional palladium diselenide. *Appl. Phys. Lett.* **114**, 253102 (2019).
30. Elghazali, M. A. *et al.* Pressure-induced superconductivity up to 13.1 K in the pyrite phase of palladium diselenide PdSe₂. *Phys. Rev. B* **96**, 060509(R) (2017).
31. Zheng, W. *et al.* Detailed study of the Fermi surfaces of the type-II Dirac semimetallic candidates XTe₂ (X = Pd, Pt). *Phys. Rev. B* **97**, 235154 (2018).
32. Fei, F. *et al.* Nontrivial Berry phase and type-II Dirac transport in the layered material PdTe₂. *Phys. Rev. B* **96**, 041201(R) (2017).
33. Leng, H., Paulsen, C., Huang, Y. K. & De Visser, A. Type-I superconductivity in the Dirac semimetal PdTe₂. *Phys. Rev. B* **96**, 220506(R) (2017).
34. Liu, W. *et al.* Enhanced superconductivity in the Se-substituted 1T-PdTe₂. *Phys. Rev. Mater.* **5**, 14802 (2021).
35. Gantmakher, V. F. *electrons and disorder in solids*. (Oxford University Press, 2005).
36. Mott, N. F. & Davis, E. A. *Electronic processes in non-crystalline materials*. (Oxford university press, 2012).
37. Yu, Z. G. & Song, X. Variable range hopping and electrical conductivity along the DNA double helix. *Phys. Rev. Lett.* **86**, 6018–6021 (2001).
38. Han, M. Y., Brant, J. C. & Kim, P. Electron transport in disordered graphene nanoribbons. *Phys. Rev. Lett.* **104**, 056801 (2010).

39. Qiu, H. *et al.* Hopping transport through defect-induced localized states in molybdenum disulphide. *Nat. Commun.* **4**, 2642 (2013).
40. Amit & Singh, Y. Heat capacity evidence for conventional superconductivity in the type-II Dirac semimetal PdTe₂. *Phys. Rev. B* **97**, 054515 (2018).
41. Toby, B. H. & Von Dreele, R. B. GSAS-II : the genesis of a modern open-source all purpose crystallography software package. *J. Appl. Crystallogr.* **46**, 544–549 (2013).
42. Kresse, G. & Furthmüller, J. Efficient iterative schemes for ab initio total-energy calculations using a plane-wave basis set. *Phys. Rev. B* **54**, 11169–11186 (1996).
43. Dion, M., Rydberg, H., Schröder, E., Langreth, D. C. & Lundqvist, B. I. Van der Waals density functional for general geometries. *Phys. Rev. Lett.* **92**, 246401 (2004).
44. Klimeš, J., Bowler, D. R. & Michaelides, A. Chemical accuracy for the van der Waals density functional. *J. Phys. Condens. Matter* **22**, 022201 (2010).

Acknowledgments

This work at University of Texas at Dallas is supported by US Air Force Office of Scientific Research Grant No. FA9550-19-1-0037 and National Science Foundation (DMR-1921581). We also acknowledge the support from Office of Research at University of Texas at Dallas through Seed Program for Interdisciplinary Research (SPIRe) and the Core Facility Voucher Program. The project or effort depicted is sponsored by the Department of Defense, Defense Threat Reduction Agency. The content of the information does not necessarily reflect the position or the policy of the federal government, and no official endorsement should be inferred.

Table 1. Crystallographic Data, Atomic Coordinates and Equivalent Isotropic Displacement Parameters of PdSe_{1.2}Te_{0.8}

| | | | | | | |
|------------------------------------|---|------------|------------|------------|----------|--|
| Temperature | 295 K | | | | | |
| Wavelength | 0.71073 Å | | | | | |
| Cell parameters | $a = 11.2450(9)$ Å, $b = 4.1877(4)$ Å, $c = 6.8110(5)$ Å $\beta = 124.326(2)$, $V = 264.88(4)$ Å ³ , $Z = 4$ | | | | | |
| Space group | C2/c (No. 15) | | | | | |
| Absorption coefficient | 31.834 mm ⁻¹ | | | | | |
| F (000) | 511.4 | | | | | |
| θ range for data collection | 4.389 - 32.921 | | | | | |
| Reflections collected | 2302 | | | | | |
| Independent reflections | 487 [[R _{int}] = 0.0139] | | | | | |
| Data/restraints/parameters | 487/0/18 | | | | | |
| Goodness-of-fit on F ² | 1.104 | | | | | |
| Final R indices [I > 2σ(I)] | R ₁ = 0.0225, wR ₂ = 0.0623 | | | | | |
| R indices (all data) | R ₁ = 0.0228, wR ₂ = 0.0624 | | | | | |
| Largest diff. peak and hole | 3.854 and -1.249 e·Å ⁻³ | | | | | |
| atom | Wyckoff site | x | y | z | Occ. | U _{eq} ^a (Å ²) |
| Pd1 | 4c | 3/4 | 1/4 | 1/2 | 1 | 0.0120(2) |
| Se1 | 8f | 0.60958(3) | 0.31783(9) | 0.05186(5) | 0.615(8) | 0.0133(2) |
| Te1 | 8f | 0.60958(3) | 0.31783(9) | 0.05186(5) | 0.385(8) | 0.0133(2) |

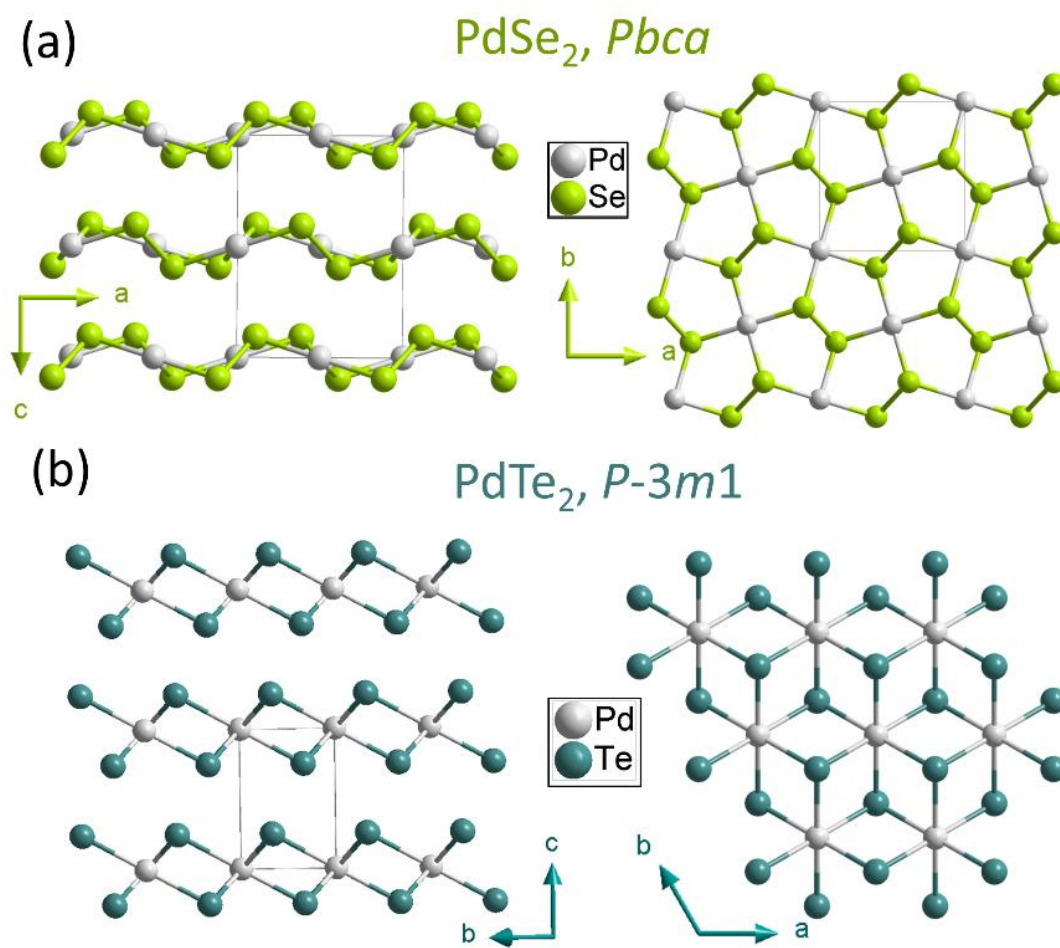


Fig. 1 Ball and stick models of (a) PdSe_2 and (b) PdTe_2 side view (left) and top view (right).

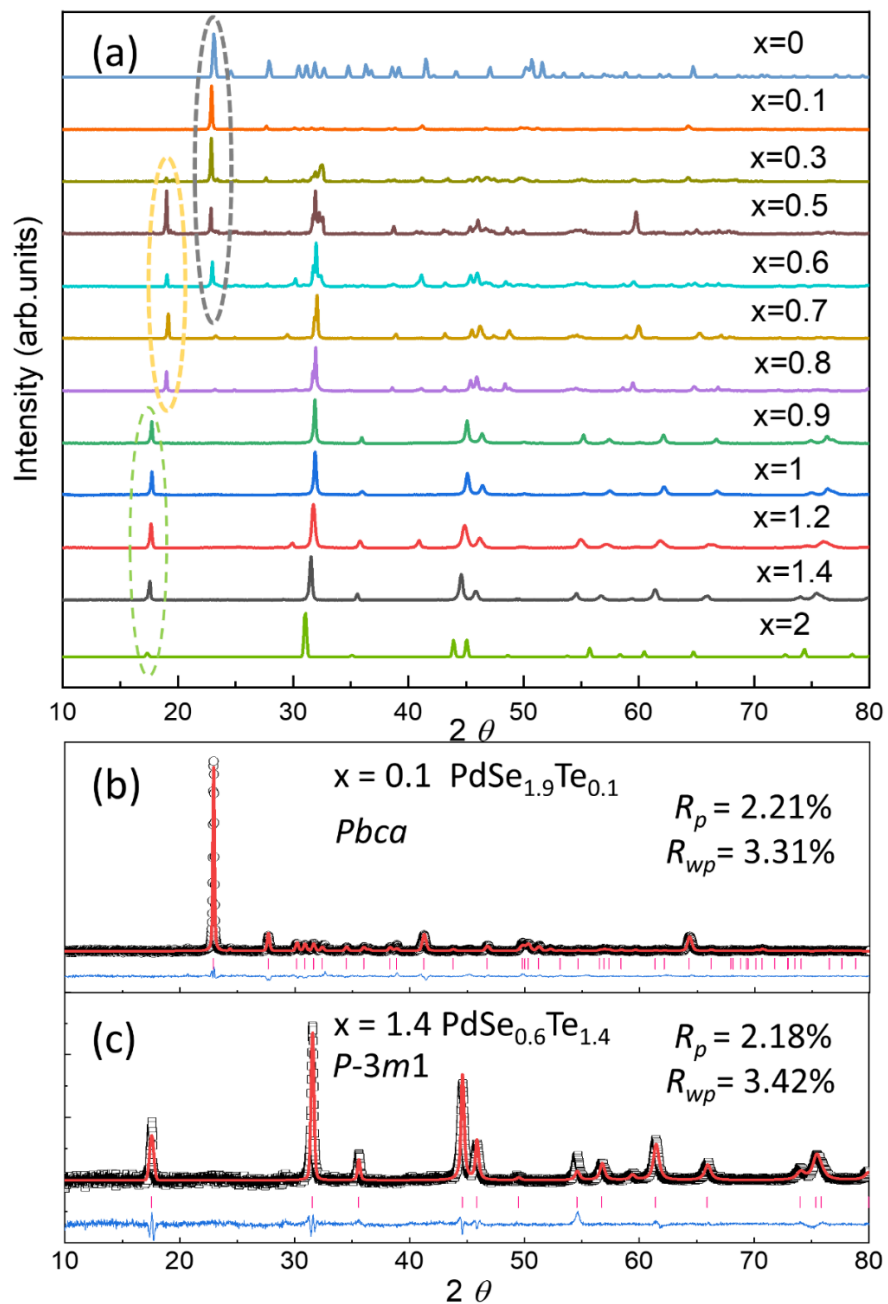


Fig. 2 (a) Powder X-ray diffraction patterns of $\text{PdSe}_{2-x}\text{Te}_x$ ($0 \leq x \leq 2$). (b) Rietveld refinement for $\text{PdSe}_{1.9}\text{Te}_{0.1}$ and (c) $\text{PdSe}_{0.6}\text{Te}_{1.4}$. The black circulars, red lines, pink bars, blue lines denote the observed diffraction intensities, calculated diffraction intensities, calculated locations of diffraction peaks and the difference between the calculated and observed diffraction intensities, respectively.

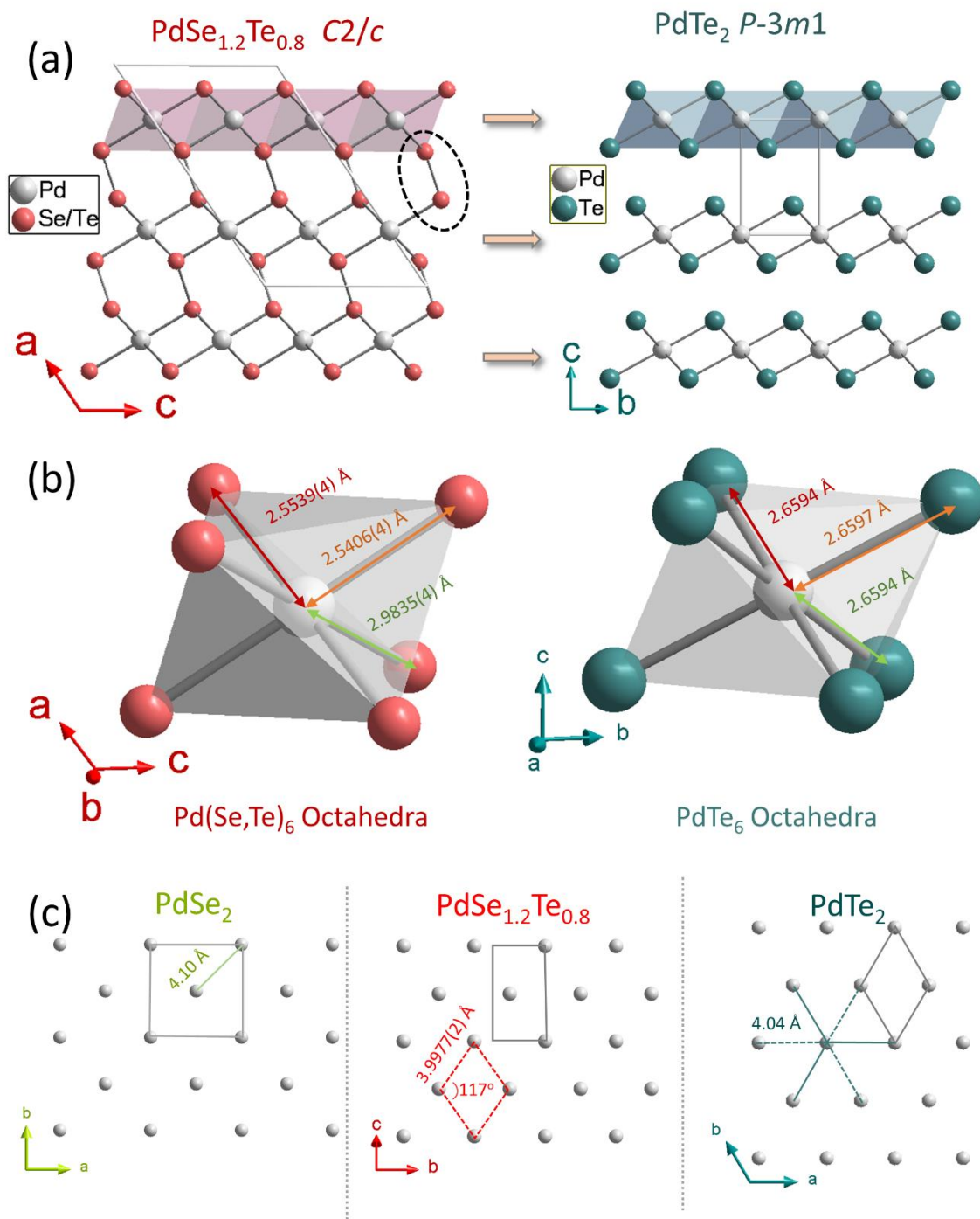


Fig. 3 (a) Ball and stick models for PdSe_{1.2}Te_{0.8} with space group C2/c along different directions. (b) Comparison of octahedra in PdSe_{1.2}Te_{0.8} and PdTe₂ structures. (c) Metal configurations in Pd planes of PdSe₂, PdSe_{1.2}Te_{0.8} and PdTe₂.

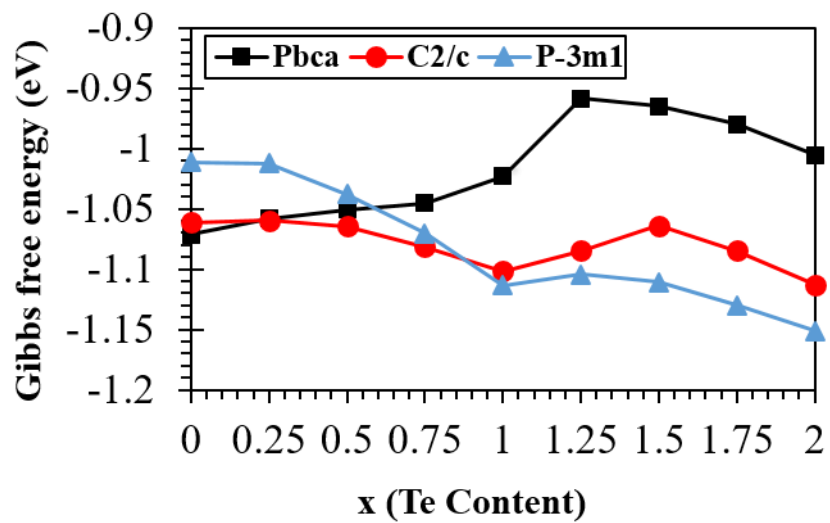


Fig. 4: Formation energy (Gibbs free energy) of *Pbca*, *C2/c* and *P-3m1* phases of $\text{PdSe}_{2-x}\text{Te}_x$ at 300K, calculated using DFT.

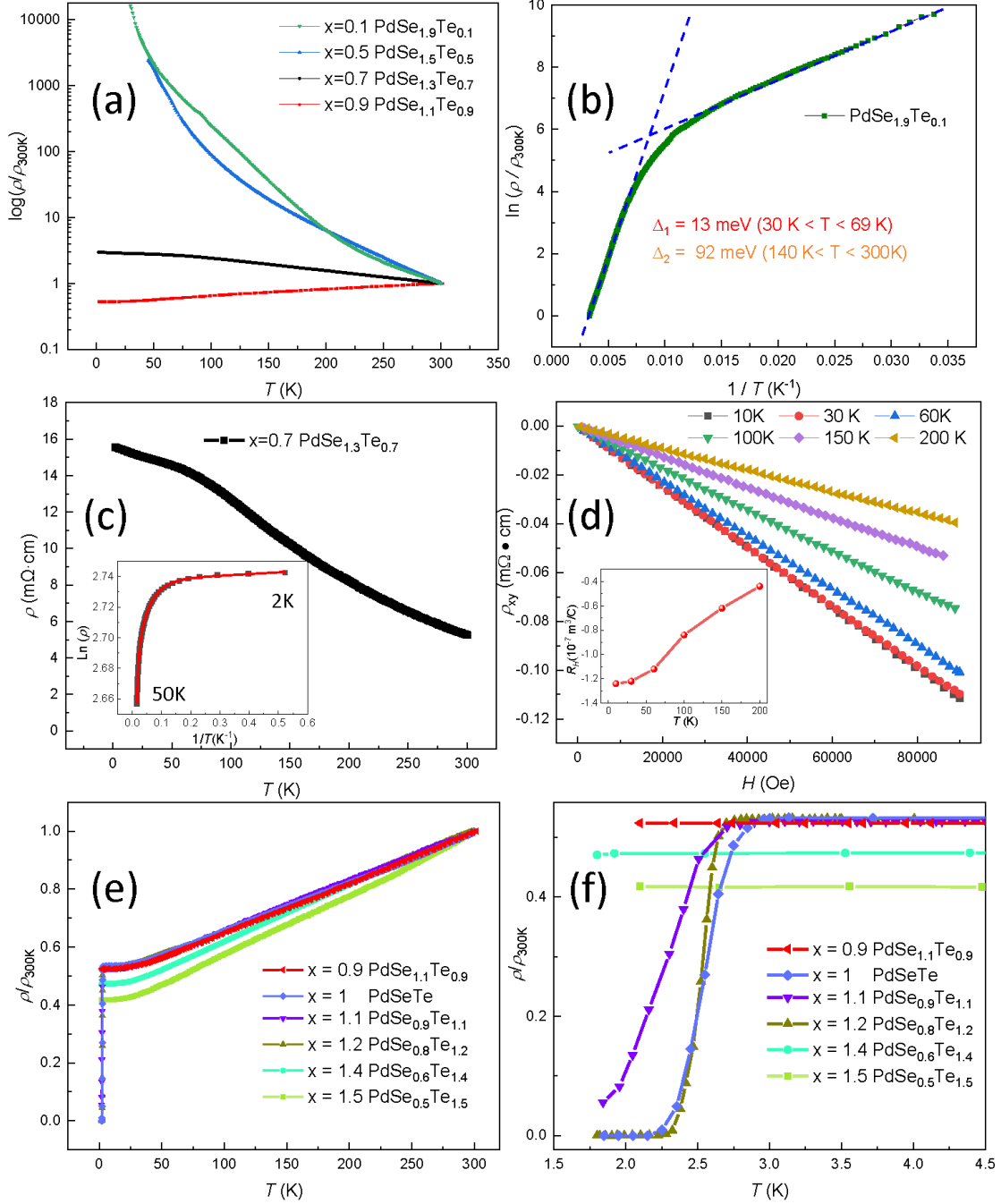


Fig. 5 (a) Temperature dependence of normalized resistivity (ρ / ρ_{300K}) in log scale for $\text{PdSe}_{2-x}\text{Te}_x$ solid solution with $0.1 \leq x \leq 0.9$. (b) $\ln(\rho / \rho_{300K})$ vs $(1/T)$ for $\text{PdSe}_{1.9}\text{Te}_{0.1}$. The blue dashed lines represent the fitting using the standard activation model. (c) Electrical resistivity ρ vs. temperature T for $\text{PdSe}_{1.3}\text{Te}_{0.7}$. The inset shows $\ln(\rho)$ vs. $(1/T)$ of $\text{PdSe}_{1.3}\text{Te}_{0.7}$ in the temperature range 2 - 50 K. The solid red line is fitted to Eq.1. (d) Hall resistivity of $\text{PdSe}_{1.3}\text{Te}_{0.7}$ at 10K, 30K, 60 K, 100 K,150 K and 200K. The inset shows the evolution of the Hall coefficient R_H with temperature. (e) Temperature-dependent normalized resistance (R/R_{300K}) of $\text{PdSe}_{2-x}\text{Te}_x$ solid solution for $0.9 \leq x \leq 1.5$. (f) Enlarged view of R/R_{300K} in the low temperature region 1.8 – 4.5 K.

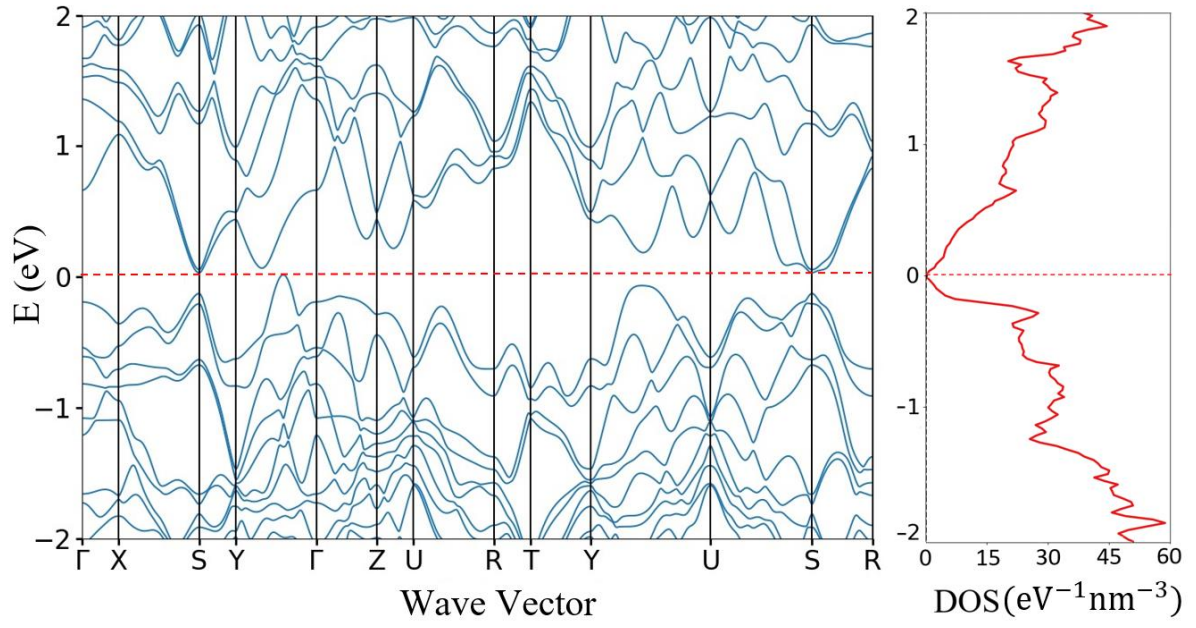


Fig. 6: Band structure and density-of-states of PdSe_{1.25}Te_{0.75} determined from first principles.

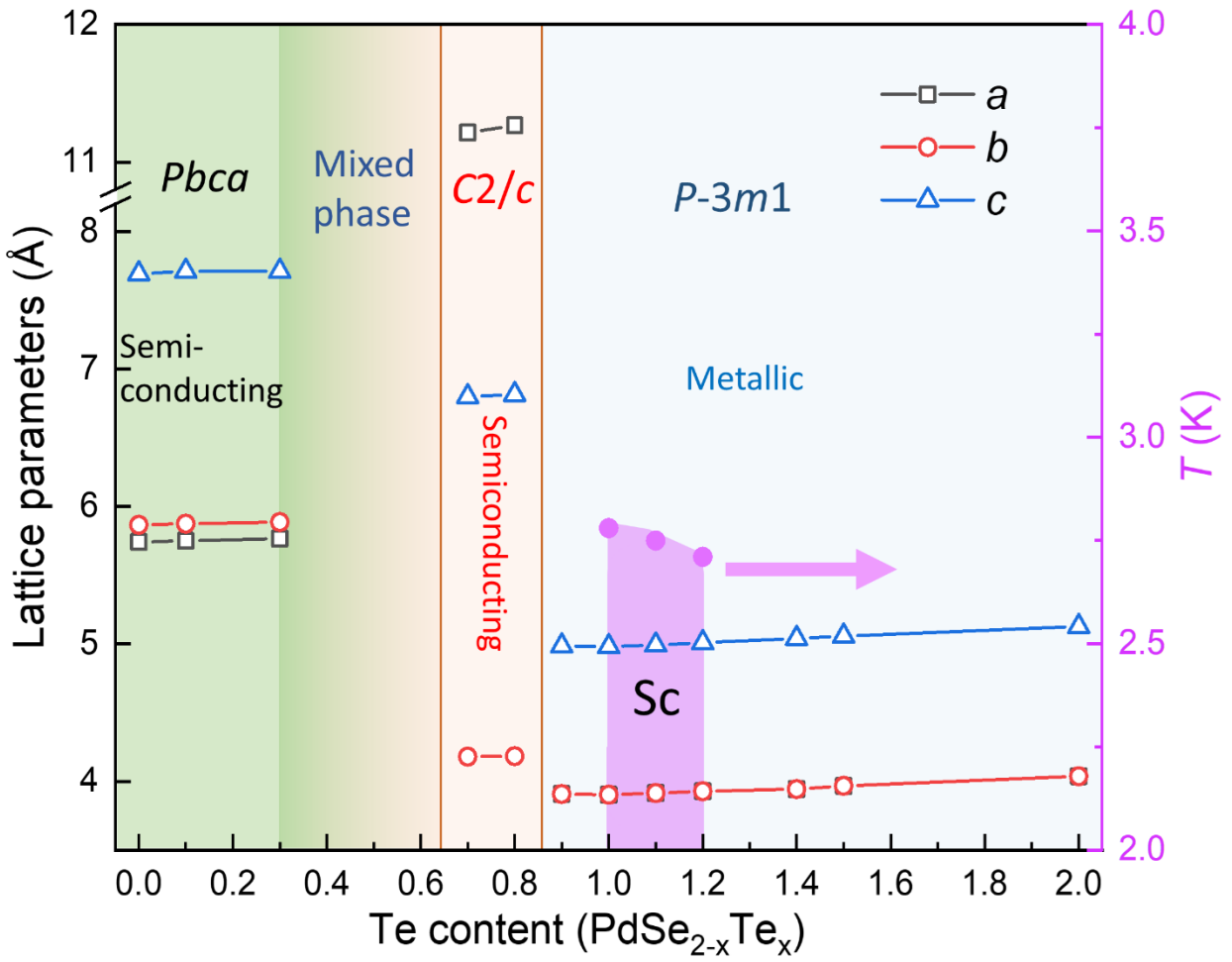


Fig. 7 Phase diagram of $\text{PdSe}_{2-x}\text{Te}_x$ versus Te content x . Sc denotes superconducting phase. Open squares, circulars and triangles show the lattice parameters a , b and c respectively. Solid purple balls show the onset superconducting transition temperature determined from transport measurements.